The distribution and kinematics of early high-σ peaks in present-day haloes: implications for rare objects and old stellar populations

Jürg Diemand,[1,2]⋆ Piero Madau[1] and Ben Moore[2]

[1]*Department of Astronomy and Astrophysics, University of California, Santa Cruz, CA 95064, USA*
[2]*Institute for Theoretical Physics, University of Zürich, Winterthurerstrasse 190, CH-8057 Zürich, Switzerland*

ABSTRACT

We show that the hierarchical assembly of cold dark matter haloes preserves the memory of the initial conditions. Using *N*-body cosmological simulations, we demonstrate that the present-day spatial distribution and kinematics of objects that formed within *early* ($z \gtrsim 10$) protogalactic systems (old stars, satellite galaxies, globular clusters, massive black holes, etc.) depends mostly on the rarity of the peak of the primordial density field to which they originally belonged. Only for objects forming at lower redshifts does the exact formation site within the progenitor halo (e.g. whether near the centre or in an extended disc) become important. In present-day haloes, material from the rarer early peaks is more centrally concentrated and falls off more steeply with radius compared to the overall mass distribution, has a lower velocity dispersion, moves on more radial orbits, and has a more elongated shape. Population II stars that formed within protogalactic haloes collapsing from $\geqslant 2.5\sigma$ fluctuations would follow today an $r^{-3.5}$ density profile with a half-light radius of 17 kpc and a velocity anisotropy that increases from isotropic in the inner regions to nearly radial at the halo edge. This agrees well with the radial velocity dispersion profile of Galaxy halo stars from the recent work of Battaglia et al. and with the anisotropic orbits of nearby halo stars.

Key words: methods: *N*-body simulations – Galaxy: halo – Galaxy: kinematics and dynamics – galaxies: formation – galaxies: haloes – galaxies: star clusters.

1 INTRODUCTION

In a universe where cold dark matter (CDM) dominates structure formation, the haloes of galaxies and clusters are assembled via the hierarchical merging and accretion of smaller progenitors (e.g. Lacey & Cole 1993). This process causes structures to relax violently to a new equilibrium by redistributing energy among the collisionless mass components. Early stars formed in these progenitors behave as a collisionless system just like the dark matter particles in their host haloes, and they undergo the same dynamical processes during subsequent mergers and the buildup of larger systems like massive galaxies or clusters. It is of crucial importance in galaxy formation studies to explore the efficiency of the mixing process and to see if any spatial or kinematical signatures exist in material that collapses at different epochs and within peaks of the primordial Gaussian density field of different rarity.

In this paper, we use a suite of high-resolution cosmological *N*-body simulations to analyse the distribution and kinematics within present-day galaxy haloes of dark matter particles that originally belonged to selected branches of the merger tree. These prop-

erties are particularly relevant for the baryonic tracers of early CDM structures, e.g. the old stellar halo which may have originated from the disruption at high redshift of numerous dwarf protogalaxies (Bullock, Kravtsov & Weinberg 2000), the old halo globular clusters, and also giant ellipticals (Gao et al. 2004). The end-product of the entire merger tree is a triaxial cuspy dark matter halo (Dubinski & Carlberg 1991; Navarro, Frenk & White 1996; Moore et al. 1999; Diemand et al. 2005): a small fraction of early progenitor systems survive the merging process and end up as dark matter substructures (Ghigna et al. 1998). Since rare, early haloes are strongly biased towards overdense regions (e.g. Cole & Kaiser 1989; Sheth & Tormen 1999), i.e. towards the centres of larger-scale fluctuations that have not collapsed yet, we might expect that material originating from the earliest branches of the merger tree is today much more centrally concentrated than the overall halo. Indeed, a 'non-linear' peak biasing has been discussed previously by several authors (Moore et al. 1998; White & Springel 2000; Moore 2001).

Here we show that the distribution and kinematics of 'old material' within present-day galaxy haloes depends primarily on the rareness of the peaks of the primordial density fluctuation field to which it originally belonged. Specifically, today's properties of objects that formed in old rare density peaks above $\nu\sigma(M, z)$ depend largely on ν and not on the particular values of z and M. [Here

⋆E-mail: diemand@ucolick.org

$\sigma(M, z)$ is the rms fluctuation in the density field linearly extrapolated to redshift z smoothed with a top-hat filter of mass M. A '1σ peak' corresponds to the characteristic mass $M_*(z)$ and $\sigma(M_*, z) \simeq$ 1.69.] Such centrally concentrated components are isotropic in the inner part, just like the host galaxy haloes, but rapidly become more radially anisotropic further out.

The plan of the paper is as follows. In Section 2 we describe the numerical simulations and how to define and trace high-σ particle subsets. In Section 3 we analyse the present-day distribution of these subsets. We derive a simple empirical fitting formula for $\rho(r, \nu)$, the mass-density profile of all progenitors above $\nu\sigma$, which approximates the results of our N-body cosmological simulations for $1 < \nu < 4$. Section 4 discusses the implications of our findings for old stellar populations. We argue that such centrally concentrated components are predicted to be isotropic in the inner part, just like the host galaxy halo, but rapidly become more radially anisotropic further out. This is quantitative with the radial velocity dispersion profile of Galaxy halo stars from Battaglia et al. (2005) and with the anisotropic orbits of nearby halo stars ($\beta \simeq 0.5$; Chiba & Beers 2000). Finally, we present our conclusions in Section 5.

2 METHOD

We identify collapsed high-σ peaks at different epochs within high-resolution cosmological N-body simulations, mark them, and analyse the distribution and kinematics of this material at redshift zero. Details about the simulations and halo finding method are given in the next two subsections.

2.1 Simulations

The simulations have been performed using PKDGRAV, a parallel N-body tree code written by Stadel and Quinn (Stadel 2001): cosmological and numerical parameters are the same as in Diemand, Moore & Stadel (2004c). The present-day haloes that we analyse are labelled 'D12' (cluster) and 'G0' to 'G3' (galaxies). We also analyse an additional smaller galaxy halo ($M_{\rm vir} = 10^{11}$ M$_\odot$), labelled 'G4'.

Figs 1 and 2 show the density field of the region containing the G0–G4 galaxy haloes. Most of the material belonging to high-σ peaks in the high-resolution region can be found in the four most massive galaxy haloes, while smaller structures tend not to have any progenitors that meet the selection criteria. G4 is a special, early-forming small galaxy halo (with a high concentration of $c = 18$) that contains similar fractions of high-σ material as the more massive galaxies. From Fig. 1 it is clear that G4 is not a representative system for its mass range. All 'G' haloes form in the one region of $\sim (10$ Mpc$)^3$ that was selected from a $(90$ Mpc$)^3$ box and resimulated at high resolution. The region has a mean density of 0.5 times the background density at $z = 0$. The properties of the six haloes are given in Table 1.

The cosmological parameters are $(\Omega_{\rm m}, \Omega_\Lambda, \sigma_8, h) = (0.268, 0.732, 0.7, 0.71)$. The value of $\sigma_8 = 0.9$ given in Diemand et al. (2004c) is not correct: We found that, as a result of a mistake in the normalization, our initial conditions have less power than intended. According to linear theory, mass fluctuations grow proportional to the scalefactor in a flat $\Omega_{\rm m} = 1$ universe, which is a good approximation to the adopted ΛCDM universe at $z > 2$. Therefore the scalefactor at collapse of a given halo in our simulations would be 0.78 times smaller in a $\sigma_8 = 0.9$ model. Throughout this paper, together with the collapse redshifts given for our low-σ_8 simulations, we will also state the rescaled collapse redshifts in a $\sigma_8 = 0.9$ universe using the exact growth function for an $(\Omega_{\rm m}, \Omega_\Lambda) = (0.3, 0.7)$

cosmology (see Table 2). Using a $\sigma_8 = 0.9$ resimulation of the 'D' cluster, we confirm that the $z = 0$ results (in units of the scale radius) are consistent with those of the $\sigma_8 = 0.7$ simulation when we use the $z_{0.9}$ outputs of the $\sigma_8 = 0.9$ run to select progenitor haloes.

2.2 Tracing progenitor material

Since baryonic objects (i.e. early protogalaxies, first stars) will form in the inner parts of their host gravitational potential, it is important to assess how different their $z = 0$ distribution is when only the inner part of a progenitor halo is traced. We will therefore compare the final distribution of material marked within the central regions of early haloes with the entire marked progenitor. We will show in this section that there is no difference (except of course in the traced mass fraction) if the traced objects are *early* ($z \gtrsim 10$) protogalaxies.

Progenitor haloes are identified using the friends-of-friends algorithm (FOF) (Davis et al. 1985). For simplicity we use a fixed linking length $b = 0.164$ at all output times. Our results are not sensitive to this choice. For example, at redshift 10.5 we found 52 haloes more massive than 4.35×10^9 M$_\odot$ in the high-resolution region of the galaxy simulation. When we use a linking length two or three times smaller and mark the linked material in the same 52 groups, we obviously find a smaller fraction of marked matter but very similar density profile shapes and kinematics (see Fig. 3). We also selected the cores of haloes at the same redshift by marking all particles that have a local density [calculated from a smoothed particle hydrodynamic (SPH) kernel over 32 nearest neighbours] 10^3 times higher than the mean matter density and obtained similar $z = 0$ distributions. This demonstrates that, at redshift zero, particles originating from the cores of high-σ haloes are distributed in the same way as all the progenitor halo material, and justifies our choice of using all halo particles as tracers for baryonic objects that would likely form in the very centre of their hosts. A large number of tracers give two important advantages. First, it allows us to estimate density, velocity dispersion and anisotropy profiles reliably. Secondly, it makes the results more robust against numerical effects: Since two-body relaxation completely changes the orbits of many individual particles, even in high-resolution cosmological simulations (Diemand et al. 2004a), using only one most bound particle as a tracer for (say) a Population III remnant is not a safe choice.

We have shown above that the final distribution and kinematics of particles from high-redshift, low-mass progenitor haloes is insensitive to their original location within the host potential. The orbital energy associated with the merging of these small subunits into larger systems determines the present-day distribution and dominates the relatively small differences in the orbital and potential energies of particles within their hosts. This is not true at lower redshifts and for progenitor masses closer to the mass of the $z = 0$ parent halo. For example, progenitors above 1σ marked at $z = 1.6$ (i.e. with masses above 7.4×10^9 M$_\odot$) show only mild radial and velocity bias when the entire FOF groups are marked (Fig. 4). The difference from the total dark matter distribution becomes much larger, however, if we select within these haloes only particles with overdensity greater than 10^4, as this material is more concentrated, colder and on more radial orbits (just like in the low-mass 2σ selection – see Fig. 5).

3 DISTRIBUTION AND KINEMATICS OF HIGH-σ PEAKS

We use the linear growth approximation to structure formation to calculate the masses of 4, 3.5, 3, 2 and 1σ fluctuations collapsing at a
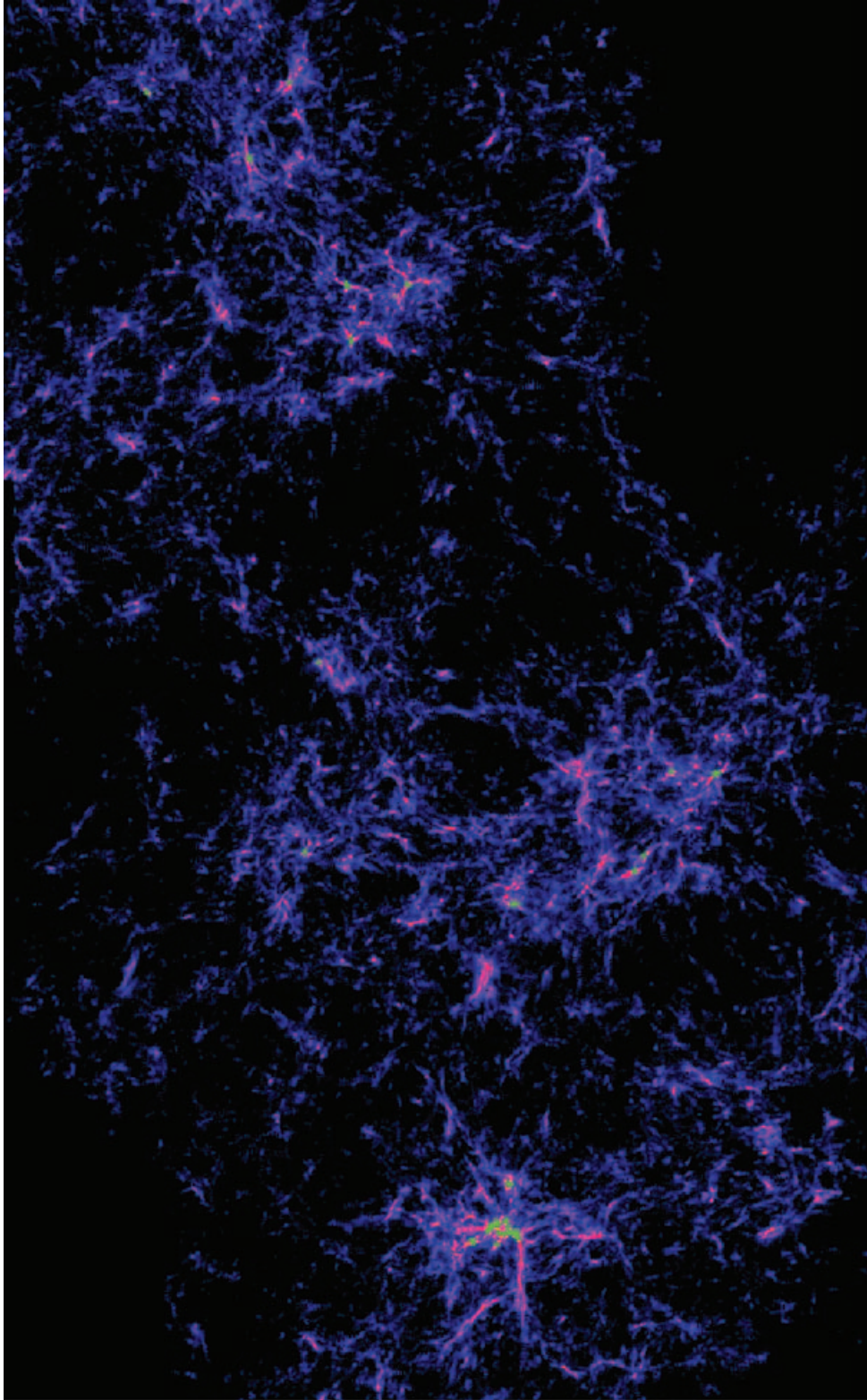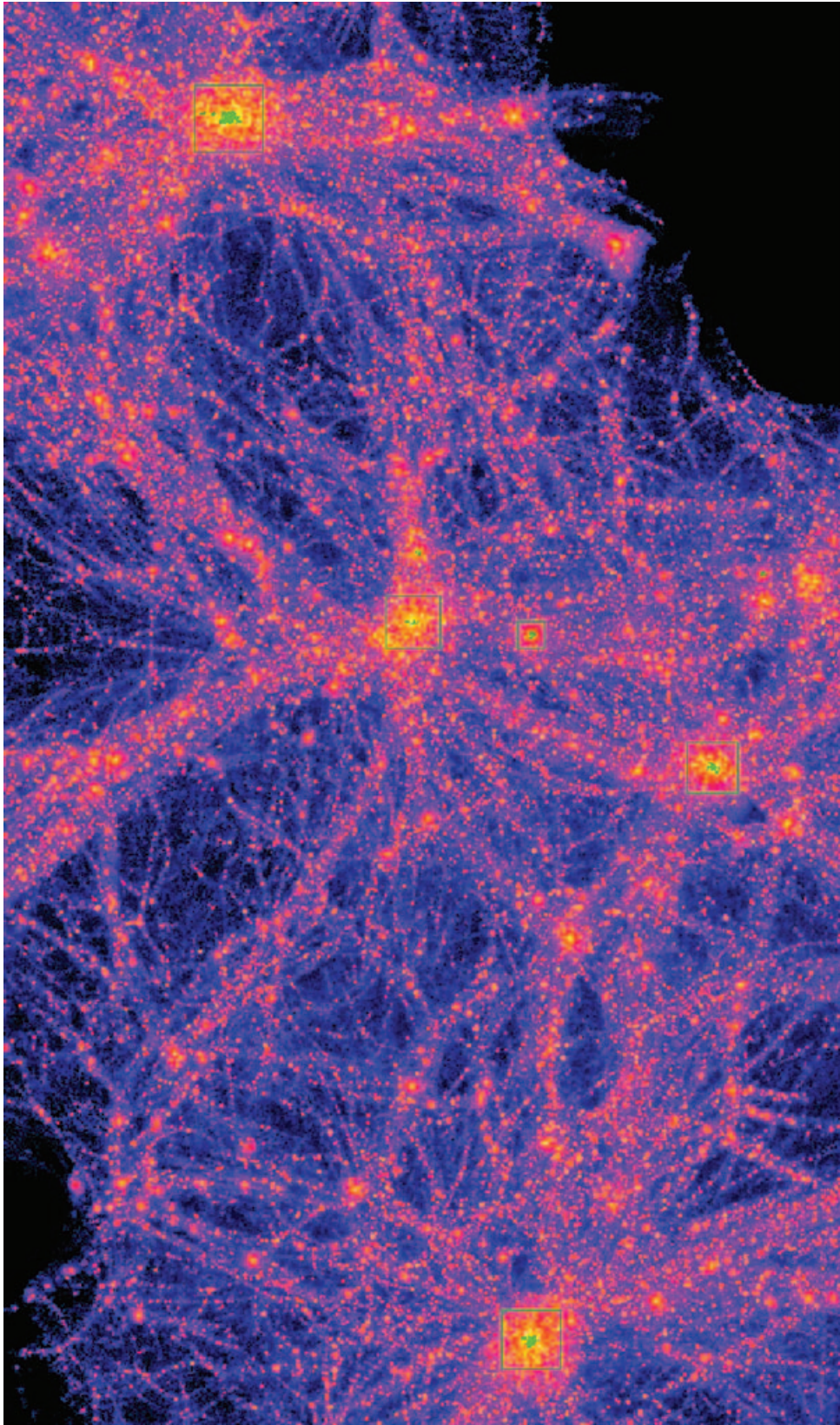
Figure 1. Density map of the high-resolution region of run G at $z = 13.7$. FOF groups more massive than $4.9 \times 10^7 \, M_\odot$ ($=84m_{DM}$) are marked in green.

given redshift. The redshifts of the simulation outputs and the halo masses corresponding to these fluctuations are given in Table 2. These values are for the cosmological model we have simulated $(\Omega_m, \Omega_\Lambda, \sigma_8, h) = (0.268, 0.732, 0.7, 0.71)$. In a $\sigma_8 = 0.9$ the same fluctuations would collapse earlier (at $z_{0.9}$, see Section 2.1).

3.1 Radial distribution

High-σ material is strongly biased towards the centre of present-day haloes (see upper panels of Figs 4–12), with the rarer peaks showing stronger bias. Figs 4–9 show different (M, z) selections

Figure 2. Density map of the high-resolution region of run G at $z = 0$. The particles marked in green were selected at $z = 13.7$ in groups above $4.9 \times 10^7 \, \mathrm{M}_\odot$ (see Fig. 1). The squares enclose the virial radii of the five galaxy haloes analysed (G0 to G4).

Table 1. Present-day properties of the six simulated dark matter haloes. The columns give halo name, spline softening length, number of particles within the virial radius, virial mass, virial radius, peak circular velocity, and radius to the peak of the circular velocity curve.

Halo	ϵ_0 (kpc)	N_{vir} (10^6)	M_{vir} ($10^{12}\,M_\odot$)	r_{vir} (kpc)	$V_{c,max}$ (km s^{-1})	$r_{V_{c,max}}$ (kpc)
D12	1.8	14.0	305	1743	958	645
G0	0.27	1.7	1.01	260	160	52.2
G1	0.27	1.9	1.12	268	162	51.3
G2	0.27	3.8	2.21	337	190	94.5
G3	0.27	2.6	1.54	299	180	45.1
G4	0.27	0.25	0.144	138	96.4	15.0

corresponding to the same value of ν. While the shapes of these profiles are similar for a given ν, the normalization (or traced mass fraction) generally grows with increasing mass threshold and lower redshifts. The density profiles are averaged over the four galaxy haloes of similar mass. The scatter from halo to halo in their total density profiles and that of their subsets is relatively small, but there are substantial halo-to-halo variations in the anisotropy parameter $\beta(r)$, which we discuss in Section 3.2.

Mass densities are fitted with a general $\alpha\beta\gamma$ profile that asymptotes to a central cusp $\rho(r) \propto r^{-\gamma}$:

$$\rho(r, \nu) = \frac{\rho_s}{(r/r_v)^\gamma \left[1 + (r/r_v)^\alpha\right]^{(\beta-\gamma)/\alpha}}. \qquad (1)$$

For comparison the NFW (Navarro, Frenk & White 1996) profile has $(\alpha, \beta, \gamma) = (1, 3, 1)$, while the Moore et al. (1999) profile has $(\alpha, \beta, \gamma) = (1.5, 3, 1.5)$. We fix $\alpha = 1$ and the inner slope to $\gamma = 1.2$, which is the best-fitting slope for the D12 cluster when resolved at very high resolution ($m_{DM} = 3.0 \times 10^5\,M_\odot$) (Diemand et al. 2005). We fit the entire dark halo using an outer slope of $\beta = 3$ to determine the scale radius $r_s = r_{vir}/c$, where c is the concentration. To approximate the high-σ subset profiles we use a smaller scale radius $r_v \equiv r_s/f_v$ (corresponding to a higher concentration $c_v \equiv f_v c$) and also a steeper outer slope β_v. The f_v and β_v values used in the plots are calculated with simple empirical formulae that approximately parametrize the entire range of profiles, i.e. peaks above 1 to 4σ and haloes ranging from a low-concentration ($c = 4.5$) cluster halo to a small, $c = 17$ galaxy halo:

$$r_v \equiv r_s/f_v, \qquad f_v = \exp(\nu/2), \qquad \beta_v = 3 + 0.26\nu^{1.6}. \qquad (2)$$

The values for the 1 to 4σ peaks are given in Table 3, and the profiles are plotted in the upper left panels of Figs 4–12 with open

Figure 3. The present-day distribution and kinematics of dark matter particles selected at $z = 10.5$, averaged over four Milky Way sized simulated haloes. We marked the 52 most massive groups found with FOF using different linking lengths: $b = 0.164$ (dotted lines), $b = 0.164/2$ (long-dashed lines) and $b = 0.164/3$ (short-dashed lines). Particles selected at the same redshift with overdensities above 1000 have similar present-day distributions (dash-dotted lines). For comparison, we also plot the same quantities using all particles from the final structure (solid curves).
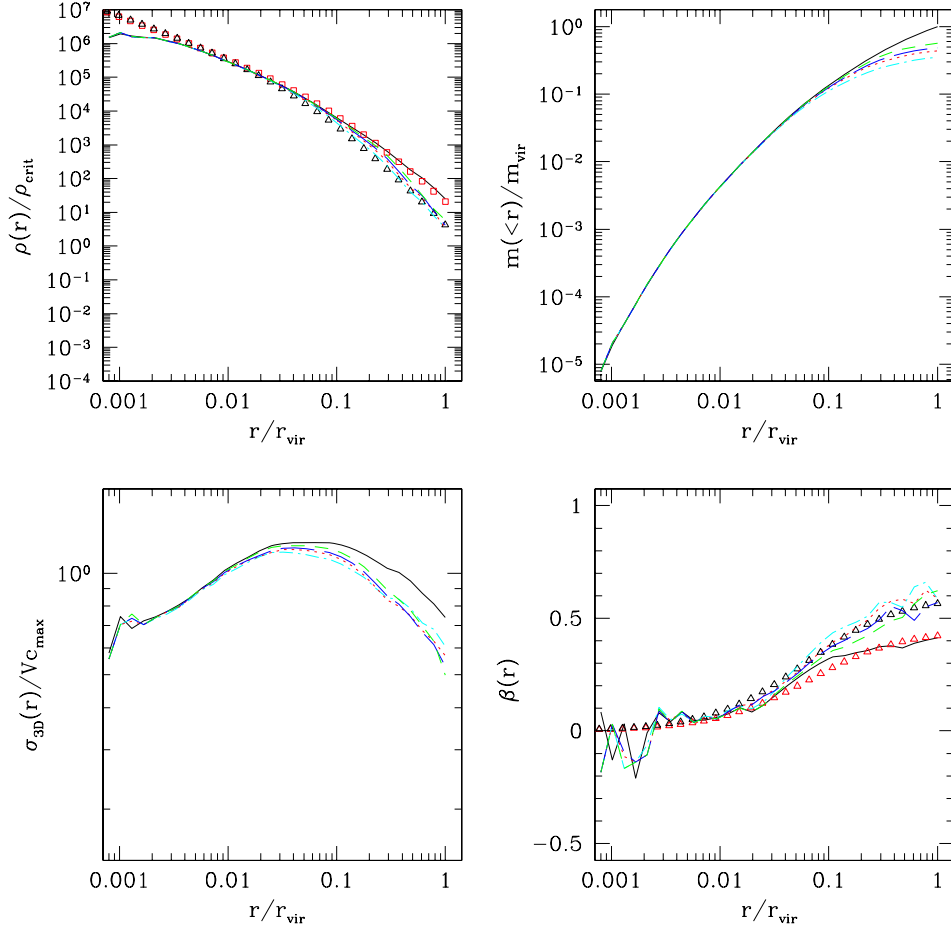
Figure 4. The present-day distribution and kinematics of peaks above 1σ averaged over four parent Milky Way sized galaxies. Here and in subsequent plots, the same-σ peaks selected at the highest and up to the next three output redshifts (given in Table 2) are plotted as dash-dotted, dotted, long-dashed and short-dashed lines, respectively. For comparison, we also plot the same quantities using all particles (solid curves). The triangles in the upper left and lower right panels show the empirical fitting functions in (2) and (8).

triangles. The fits are just approximate but they are reproduce well at least one profile for each of the ν values. Other parameters and functional forms could fit some of the data better.

For easier comparison with extragalactic observational data of old stellar or globular cluster populations, we also fitted our high-σ subset profiles with a deprojected $R^{1/4}$ law, using the accurate numerical approximation of Márquez et al. (2001):

$$\rho(r) = \rho_0 (r/R_e)^{-p} \exp\left[-b(r/R_e)^{1/4}\right], \tag{3}$$

with

$$p = 1.0 - 0.6097(1/4) + 0.05563(1/4)^2,$$

$$b = 1.9992 \times 4 - 0.3271.$$

The best-fitting effective radii R_e are given in Table 3. Like the r_ν values, they scale with r_s and not with the virial radius.

3.2 Kinematics

The lower left panels of Figs 4–12 show the three-dimensional velocity dispersion profiles $\sigma_{3D}^2 = \sigma_r^2 + \sigma_t^2$, where σ_r and σ_t are the radial and tangential velocity dispersions ($\sigma_t^2 = \sigma_\theta^2 + \sigma_\phi^2$). The lower right panels show the anisotropy parameter $\beta = 1 - 0.5\sigma_t^2/\sigma_r^2$ as a function of radius. The high-σ subsets are clearly slower and on

more radial orbits than the entire dark matter component at the same radius. As with the density profiles, the differences depend on ν, i.e. the highest σ peaks have the lowest σ_{3D} and the largest β values.

Like the density profiles, also the velocity dispersions are averaged over the four galaxy-size parent haloes. There is little halo-to-halo scatter in $\rho(r)$ and $\sigma_{3D}(r)$, but there is substantial scatter in the anisotropy parameter $\beta(r)$, especially near the virial radius. We have checked that the radial bias exists in each data set and is not just on average. The variation in β over the four galaxies is about 0.1 within 10 per cent of the virial radius, for both the parent halo and the progenitor subsets. Further out the scatter becomes much larger: particles in the parent halo (subsets) have a total spread of 0.45 (0.35) near r_{vir}.

3.2.1 Jeans equations

The origin of the smaller velocity dispersions of the subsets can be traced to the fact that high-σ peaks form closer to the main progenitor of the present-day parent halo; hence they join the system with small infall velocities and at early times when its potential well is much shallower. Since they have been part of the parent halo for a long time, they are probably in dynamical equilibrium with the host, i.e. their density and velocity profiles should be a stationary solution to the Jeans equation in the potential, $\Psi(r)$, of the parent halo. Setting

Table 2. Properties of 4, 3.5, 3, 2 and 1σ fluctuations collapsing at different output redshifts. Here N_{groups} is the number of groups found with mass $>M$, and f is the fraction of the overall mass in the high-resolution region that is inside these groups (the total mass in the high-resolution region is $3.6 \times 10^{13}\,\text{M}_\odot$ in run G, and $1.6 \times 10^{15}\,\text{M}_\odot$ in run D12). The fractions differ from the average value, $f = \text{erfc}(\nu/\sqrt{2})$, as the high-resolution regions analysed are relatively small and are not representative patches of the Universe. We did not use outputs when the mass scale lies below 10 times the particle mass, or when the number of groups is smaller than two per present-day halo. In the cluster run (D12) we have only analysed one representative case for 1 and 2σ progenitors.

ν	z	$z_{0.9}$	M_{min} (M$_\odot$)	$N_{\text{groups}} \in$ G	$f \in$ G	$N_{\text{groups}} \in$ D12	$f \in$ D12
4	10.5	13.8	3.4×10^9	–	–	24	1.2×10^{-4}
4	8.7	11.5	1.8×10^{10}	–	–	14	2.9×10^{-4}
4	7.4	9.8	6.2×10^{10}	–	–	8	5.8×10^{-4}
4	5.7	7.7	3.6×10^{11}	–	–	3	1.2×10^{-3}
3.5	16.3	21.2	5.8×10^6	72	2.5×10^{-5}	–	–
3.5	13.7	17.9	4.9×10^7	35	1.3×10^{-4}	–	–
3.5	10.5	13.8	8.4×10^8	(5)		236	3.4×10^{-4}
3.5	8.7	11.5	5.2×10^9	–	–	126	1.0×10^{-3}
3.5	7.4	9.8	1.9×10^{10}	–	–	60	1.7×10^{-3}
3.5	4.4	6.0	6.6×10^{11}	–	–	8	8.5×10^{-3}
3	13.7	17.9	5.9×10^6	670	3.0×10^{-4}	–	–
3	10.5	13.8	2.2×10^8	52	8.7×10^{-4}	1659	7.1×10^{-4}
3	8.7	11.5	1.0×10^9	23	1.6×10^{-3}	1205	2.5×10^{-3}
3	7.4	9.8	4.3×10^9	8	2.0×10^{-3}	501	4.3×10^{-3}
3	4.4	6.0	2.3×10^{11}	–	–	27	1.4×10^{-2}
2.5	10.5	13.8	1.8×10^7	1426	2.5×10^{-3}		
2.5	8.7	11.5	1.0×10^8	558	5.1×10^{-3}		
2	8.7	11.5	7.6×10^6	12740	1.1×10^{-2}	–	–
2	7.4	9.8	4.8×10^7	2657	1.5×10^{-2}	–	–
2	4.4	6.0	6.3×10^9	43	2.1×10^{-2}	2459	2.1×10^{-2}
1	2.4	3.5	4.8×10^8	1413	0.14	–	–
1	1.6	2.4	7.4×10^9	108	0.13	4258	0.24
1	1.1	1.8	3.9×10^{10}	24	0.11	–	–
1	0.8	1.5	1.0×10^{11}	9	0.11	–	–

Table 3. Density profile parameters of 4, 3.5, 3, 2.5, 2 and 1σ fluctuations in parent haloes at $z = 0$. The profiles are approximated with the general function in equation (1) using $(\alpha, \beta, \gamma) = (1, \beta_\nu, 1.2)$ and a concentration c_ν that is higher than the halo concentration c by some factor f_ν, i.e. $c_\nu \equiv f_\nu c$. The outer profile slopes β_ν and concentration factors f_ν given here are calculated from the empirical formulae in (2). These profiles are plotted in the corresponding figures as triangles. R_e is the effective radius of the deprojected $R^{1/4}$ model (equation 3) and $r_{1/2}$ is the average half-mass radius of the high-σ material at $z = 0$. Both R_e and $r_{1/2}$ are given in units of the scale radius of the entire dark matter halo (r_{vir}/c). Values in brackets are for the cluster halo D12, which has a concentration of $c = 4.5$. For comparison, the bottom line gives the same parameters for the entire halo.

ν	f_ν	β_ν	R_e	$r_{1/2}$
4	7.39	5.39	(0.067)	(0.1)
3.5	5.76	4.93	0.077	0.12 (0.18)
3	4.48	4.51	0.14	0.28 (0.28)
2.5	3.49	4.13	0.32	0.51
2	2.72	3.79	0.71	0.70 (0.83)
1	1.65	3.26	2.9	1.8 (1.2)
halo	1.0	3.0	8.3	3.5 (1.8)

time derivatives to zero and assuming spherical symmetry, the Jeans equation can be written as (Binney & Tremaine 1987)

$$\frac{\text{d}}{\text{d}r}\left(\rho\sigma_r^2\right) + \frac{2\beta}{r}\rho\sigma_r^2 + \rho\frac{\text{d}\Psi}{\text{d}r} = 0. \tag{4}$$

Approximating the anisotropy parameter as in Diemand et al. (2004c),

$$\beta(r) = \beta_{\text{vir}}(r/r_{\text{vir}})^{1/3}, \tag{5}$$

equation (4) admits the solution

$$\rho(r)\sigma_r^2(r) = G\,\text{e}^{-6\beta(r)} \int_r^\infty \text{e}^{6\beta(y)} y^{-2} \rho(y) M(y)\,\text{d}y. \tag{6}$$

Fig. 5 depicts this solution for 2σ material. We use equation (1) with $(\alpha, \beta_\nu, \gamma) = (1, 5.4, 1.2)$ and $r_\nu = r_s = r_{\text{vir}}/10$ to approximate the density profile (see long-dashed lines in Fig. 5), and equation (5) with $\beta_{\text{vir}} = 0.8$ to approximate the anisotropy profile $\beta(r)$. The radial velocity dispersion calculated from (6) is converted to σ_{3D} and plotted (filled squares) in Fig. 5. It is very close to the measured velocity dispersions, which confirms our expectation that high-σ material is a more concentrated and colder subset of particles in dynamical equilibrium within the total dark matter potential. This is just the opposite situation to the one of surviving CDM subhaloes, which are a more extended, hot subset in equilibrium with the host potential (Diemand, Moore & Stadel 2004b). We also calculated an isotropic $\beta(r) = 0$ and a constant $\beta(r) = 0.5$ model [see van den Bosch et al. 2005, for the corresponding solution of equation (4)], but the two cases do not to reproduce the measured $\sigma_{3D}(r)$ very well (see circles versus long-dashed line in the lower left panel of Fig. 5).

As a consistency check we also solve equation (6) for the entire dark matter halo, using $(\alpha, \beta_\nu, \gamma) = (1, 3, 1.2)$ and $\beta_{\text{vir}} = 0.45$
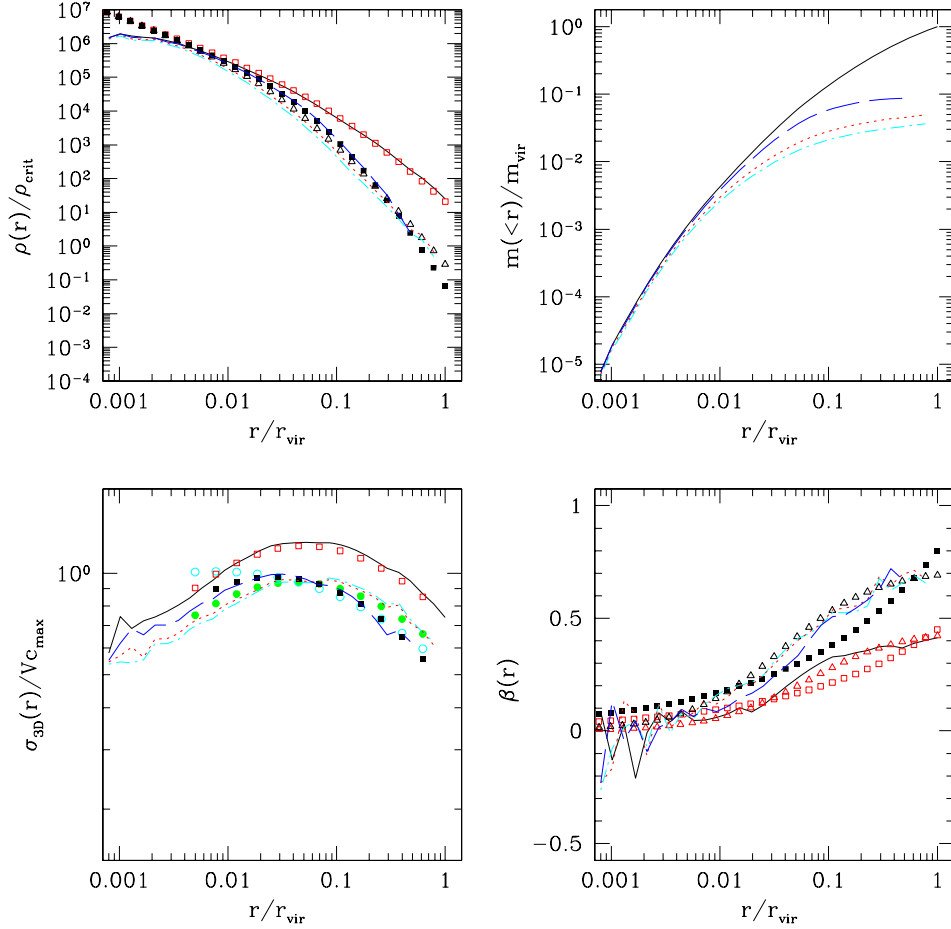
Figure 5. Distribution and kinematics of peaks above 2σ in present-day galaxy-sized haloes. Line styles are as in Fig. 4. The squares in the lower left panel are calculated from the Jeans equation (4) using approximations for $\rho(r)$ and $\beta(r)$ as input (plotted with squares in the upper left and lower right panels). Dispersions from an isotropic model (filled circles) and a model with constant radial anisotropy $\beta(r) = 0.5$ (open circles) do not fit the corresponding data (long-dashed lines) very well.

to approximate the density and anisotropy profiles. The resulting σ_{3D} is plotted (open squares) in the lower left panel of Fig. 5. The agreement with the measured dispersion is very good. As expected our average system from four isolated and relaxed galaxy haloes is very close to a stationary equilibrium solution.

3.2.2 A fitting function for $\beta(r, \nu)$

Equation (5) is not a very good approximation to the average anisotropy $\beta(r)$ of the four G0–G3 parent galaxies. The function used by Mamon & Łokas (2005),

$$\beta(r) = \beta_a \frac{r}{r + r_a}, \tag{7}$$

fits the data quite well for $\beta_a = 0.45$ and $r_a = 0.065$. For the high-σ particles the radial anisotropy is larger and sets in further inside. This behaviour is approximated by simply using the scale radii of the high-σ density profiles (2) instead of $r_a = 0.065$, and an amplitude β_a that grows with ν:

$$\beta(r, \nu) = \beta_{av} \frac{r}{r + r_{av}}, \tag{8}$$

with

$$r_{av} \equiv r_s/f_\nu, \qquad f_\nu = \exp(\nu/2), \qquad \beta_{av} = 1 - 0.4\nu^{-0.5}.$$

These anisotropy profiles are plotted with open triangles in the lower right panels of Figs 4–9. They also approximate the inner $\beta(r)$ of the haloes D12 and G4. Outside 10 per cent of the virial radius both the cluster D12 and the small galaxy G4 deviate substantially from the average $\beta(r)$ found for G0–G3.

3.2.3 Density slope–velocity anisotropy relation

Hansen & Moore (2005) have recently found a relation between the logarithmic slope of a density profile and its velocity anisotropy $\beta = \eta_1 - \eta_2(\mathrm{d} \log \rho/\mathrm{d} \log r)$ with η_1, ranging from -0.45 to 0.05 and η_2 from 0.1 to 0.35. This relation approximates values measured in a variety of equilibrium *N*-body and SPH systems, including CDM haloes. It is interesting to ask whether a similar relation also exists for our high-σ subsets of present-day galaxy haloes. By combining the fitting functions for $\rho(r, \nu)$ (equation 2) and $\beta(r, \nu)$ (equation 8), one indeed finds the same simple relation,

$$\beta(\mathrm{d} \log \rho/\mathrm{d} \log r) = -\eta_2(\gamma + \mathrm{d} \log \rho/\mathrm{d} \log r), \tag{9}$$

where $\gamma = 1.2$ is the slope of the inner density cusp ($\rho \propto r^{-1.2}$). The coefficient η_2 depends only mildly on ν. Parent CDM haloes and low-σ subsets have $\eta_2 \simeq 0.3$, while high-σ subsets have smaller values, $\eta_2 = (0.29, 0.28, 0.23, 0.19)$ for $\nu = (1, 2, 3, 4)$. The scatter around these relations is about 0.1 when $\beta < 0.5$ (i.e. in the inner
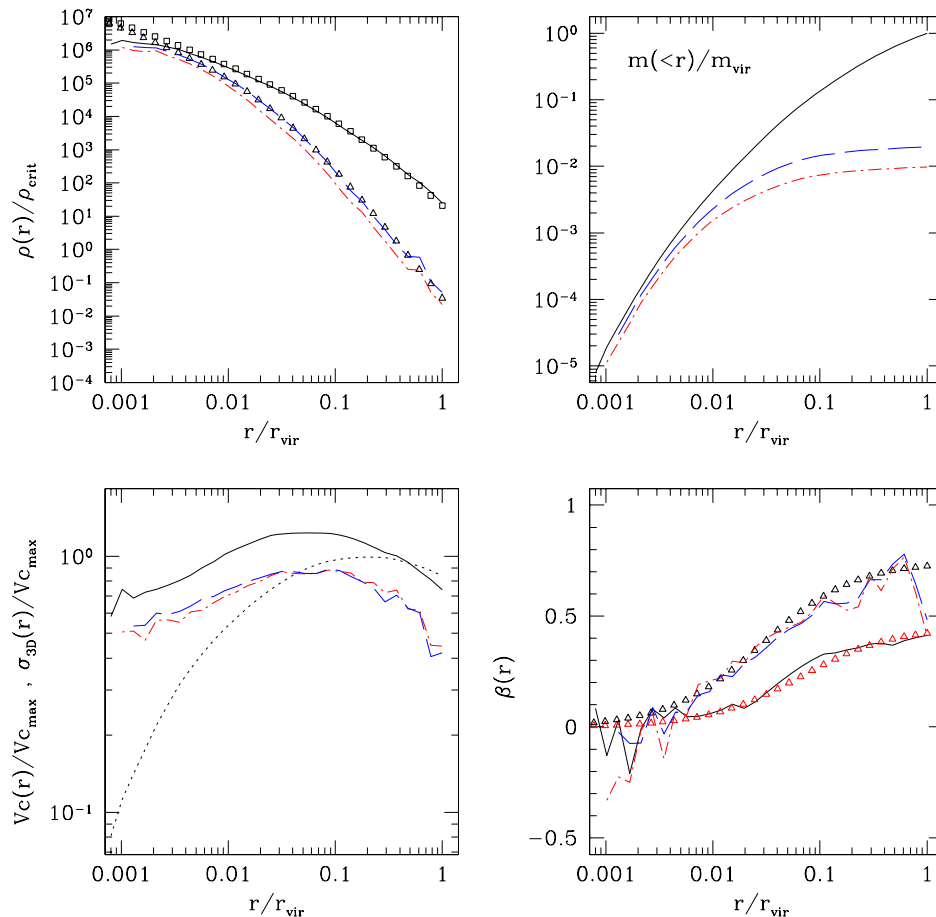
Figure 6. Distribution of peaks above 2.5σ in present-day galaxy-sized haloes. Line styles are as in Fig. 4. The distribution resembles that of the Milky Way stellar halo. In the Solar neighbourhood ($r \simeq 0.03 r_{\rm vir}$), the 3D velocity dispersion is of the order of the circular velocity [$V_{\rm c}(r)/V_{\rm c,max}$ plotted as the dotted line in the lower left panel] and there is a clear radial anisotropy, with $\beta \simeq 0.4$ (see also Fig. 10).

regions), and is larger (up to 0.4) in the outer parts. A larger, more representative sample of CDM haloes should be studied to quantify more accurately the exact slope and scatter of this important relation. The fact that even the high-σ subsets follow a nearly universal relation between velocity anisotropy and density slope supports the existence of a fundamental connection between the two quantities (Hansen & Moore 2005). This relation breaks the mass–anisotropy degeneracy present when one uses the line-of-sight velocities of extragalactic stellar halo objects (such as globular clusters) to infer total dynamical masses.

3.3 Shape of high-σ material

The axial ratios a/c and b/c are calculated with TIPSY[1] using the technique described in Katz (1991). First, the inertia tensors of the particles within a sphere of a given radius are calculated and diagonalized; then the same is done iteratively for particles within the triaxial shape found in the previous step, until the procedure converges. Note that the shape at a given radius depends on all particles within this radius, but for density profiles less steep than $\rho(r) \propto r^{-4}$ the outer particles dominate over the inner ones in the contribution to the inertia tensor.

The average axial ratios of the four galaxy haloes G0–G3 at the virial radius ($a/c \simeq 0.6$, $a/b \simeq 0.7$) are close to the mean values of

large samples of haloes (Jing & Suto 2002; Faltenbacher et al. 2002; Bailin & Steinmetz 2005). Fig. 7 shows the average shapes of 2, 3 and 3.5σ material at the present epoch. Both axial ratios become smaller for higher-σ material at all radii. (This is also true for each of the four galaxies individually, not just for the average.) This result is consistent with the finding of Jing & Suto (2002) that the average axial ratios decrease with redshift, although our 2σ haloes formed at higher redshift and lower virial mass than the range probed by Jing & Suto (2002). The origin of the extremely prolate shape of the high-σ subsets ($a : b : c \simeq 3 : 1 : 1$ for the 3.5σ material) could be a series of correlated head-on (i.e. low angular momentum) mergers along a filament aligned with the long axis (Moore et al. 2004).

For the total dark matter halo the orientations of the axes change with radius, as found in Jing & Suto (2002), and a similar behaviour is observed for the high-σ subsets. The highest-σ subsets show a slightly better alignment, which is simply explained with the fact that inner particles dominate the shape calculation due to the very high concentrations of these subsets. Between the different subsets the axes are generally well aligned only when they have many particles in common, i.e. in the inner parts. As the fraction of high-σ material drops with increasing radius, the alignment with the shape of the whole halo becomes worse.

3.4 Mass fraction of high-σ material

It is well known that high-σ peaks at early times are biased towards overdense regions where larger haloes will form later (see

---

[1] Available at: http://www-hpcc.astro.washington.edu/
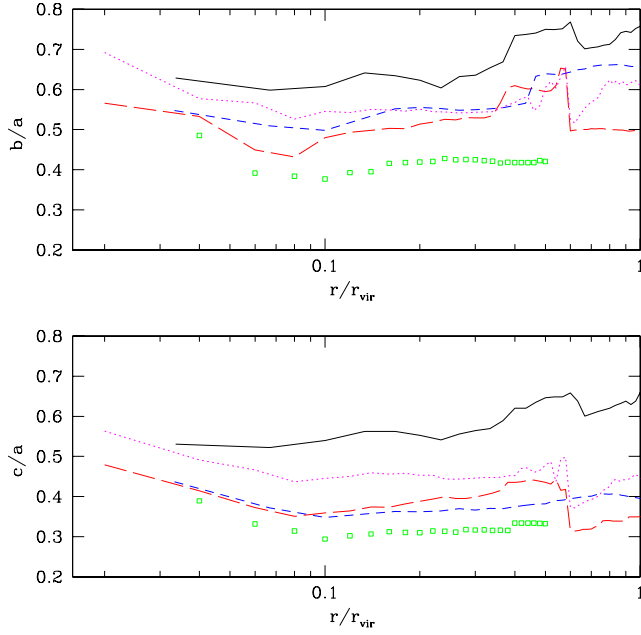
Figure 7. Shape profiles of high-σ subsets at $z = 0$ averaged over four galaxy haloes. The shapes are plotted for 3.5σ [groups with virial mass $\geqslant 4.9 \times 10^7\,M_\odot$ at $z = 13.7$ (squares)], 3σ [$\geqslant 5.9 \times 10^6\,M_\odot$ at $z = 13.7$ (long-dashed lines); and $\geqslant 2.2 \times 10^8\,M_\odot$ at $z = 10.5$ (short-dashed lines)] and 2σ material [$\geqslant 4.8 \times 10^7\,M_\odot$ at $z = 7.5$ (dotted lines)]. The axial ratios of the entire dark matter halo are plotted with solid lines.

Figs 1 and 2). How large is the mass fraction of such peaks within present-day haloes, and how does this fraction depend on the mass of the $z = 0$ parent host? Do haloes that correspond to higher-σ peaks today (like massive clusters) contain a larger fraction of early high-σ material? This question is not well defined, since the fraction of particles from peaks above 2σ in a present-day galaxy halo grows when the peaks are selected with a larger mass threshold at lower redshift (see upper right panel of Fig. 5). Here we use fixed mass threshold/redshift pairs to select progenitors and compare the mass fractions they contribute to parent haloes of different sizes. The selection of a fixed progenitor mass may be motivated in studies of old stellar populations if, for example: (a) Population III stars form in 'minihaloes' above a *molecular cooling mass*, i.e. massive enough to allow efficient gas cooling via rotovibrational levels of H_2, $M > M_{H_2} \approx 6 \times 10^5\,[(1+z)/20]^{-3/2}\,M_\odot$ (virial temperatures >2000 K); and (b) metal-poor halo stars (Population II) and globular clusters form in haloes above an *atomic cooling mass*, i.e. massive enough to allow efficient gas cooling and fragmentation via excitation of hydrogen Lyα, $M > M_H \approx 10^8\,[(1+z)/10]^{-3/2}\,M_\odot$ (virial temperature $>10^4$ K).

To test whether, at the present epoch, massive clusters contain a different fraction of high-σ material than field galaxies, we have used a lower-resolution *N*-body simulation (300^3 particles in a 90 Mpc box, for a resolution of $10^9\,M_\odot$) in order to obtain a larger galaxy/cluster sample. We have selected 10 parent hosts at $z = 0$ with FOF masses close to 2×10^{11}, 10^{12}, 10^{13} and $10^{14}\,M_\odot$, for a total of 40 haloes. We have then marked FOF groups with more than 100 particles at redshifts 7.0, 4.3, 3.1 and 0.8, and determined the fractions of the virial mass of the parent belonging to a fixed progenitor mass/redshift (M, z) pair. The values obtained are given in Table 4. The mass fractions are practically constant for all parents that host any of the selected progenitors. As we select parents of lower masses, the number of parents hosting rarer (higher-σ) progenitors drops from 10 to 0 within about a decade in mass.
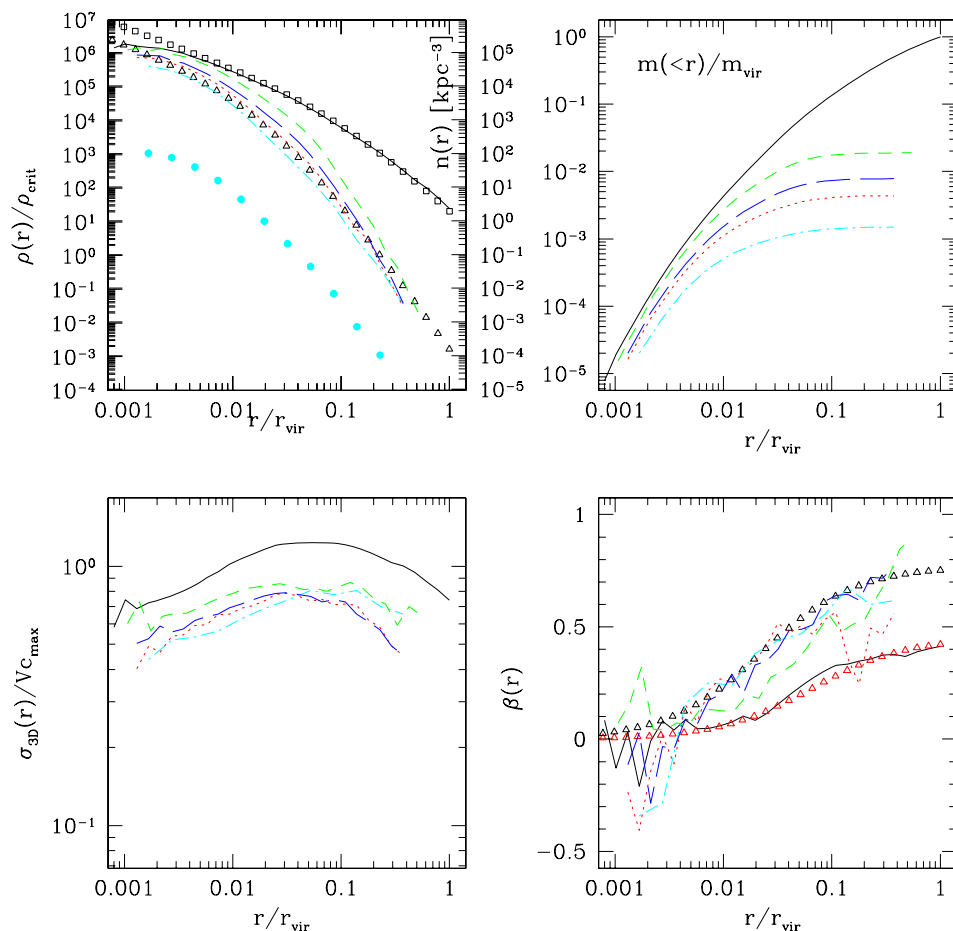
4 SOME APPLICATIONS

We have shown that the final distribution and kinematics of dark matter particles selected from early branches of the merger tree are systematically different from those of the parent halo as a whole. These properties are also relevant for old stellar populations if these form predominantly in early low-mass progenitor haloes, as stars behave essentially as collisionless systems just like the dark matter particles in our simulations. In the following we briefly discuss a number of possible applications.

4.1 Remnants of the first stars

Numerical simulations performed in the context of hierarchical structure formation theories suggest that the first (Population III) stars may have formed out of metal-free gas in dark matter minihaloes of mass above $6 \times 10^5\,M_\odot$ (Abel, Bryan & Norman 2000; Bromm, Coppi & Larson 2002; Yoshida et al. 2003; Kuhlen & Madau 2005) condensing from rare high-σ peaks of the primordial density fluctuation field at $z > 20$, and were probably very massive. Barring any fine tuning of the initial mass function (IMF) of Population III stars, intermediate-mass black holes (IMBHs) (with masses above the 5–20 $M_\odot$ range of known 'stellar-mass' holes) may be one of the inevitable end-products of the first episodes of pre-galactic star formation (Madau & Rees 2001).

Where do relic pre-galactic IMBHs lurk in present-day galaxy haloes? To shed some light on this question, we have populated our 3σ (3.5σ) simulated progenitors at $z_{0.9} = 17.9$ ($z_{0.9} = 21.2$) with one seed IMBH for every 6×10^5 solar masses of halo material. As discussed by Volonteri, Haardt & Madau (2003), these IMBHs will undergo a variety of processes during the hierarchical buildup of larger and larger haloes, like gas accretion, binary hardening, black hole mergers and triple interactions. While we neglect all of these effects here, our dark matter simulations do correctly model the bias in the formation sites, the accretion into larger haloes, and the

Table 4. Mean fractional mass in present-day parent haloes of different size (2×10^{11}, 10^{12}, 10^{13} and $10^{14}\,M_\odot$) contributed by a fixed progenitor minimum mass/redshift ($M_{\min}$, z) selection. Only parents hosting at least one selected progenitor are included when computing average values and scatter. The number of parent haloes (out of 10) with selected progenitors is given in square brackets.

$M_{\min}, z$	$10^{10}\,M_\odot, 7.0$	$10^{10}\,M_\odot, 4.3$	$10^{10}\,M_\odot, 3.1$	$10^{11}\,M_\odot, 4.3$	$10^{11}\,M_\odot, 3.1$	$10^{11}\,M_\odot, 0.8$
ν	3.2	2.1	1.6	2.75	2.07	1.0
$2 \times 10^{11}\,M_\odot$	0.0 [0]	0.049 [3]	0.158 ± 0.075 [5]	0.0 [0]	0.0 [0]	0.567 ± 0.071 [6]
$10^{12}\,M_\odot$	0.0 [0]	0.047 ± 0.035 [8]	0.149 ± 0.068 [10]	0.0 [0]	0.123 [3]	0.598 ± 0.074 [10]
$10^{13}\,M_\odot$	0.0033 ± 0.0028 [8]	0.077 ± 0.028 [10]	0.183 ± 0.040 [10]	0.036 ± 0.025 [9]	0.111 ± 0.045 [10]	0.539 ± 0.077 [10]
$10^{14}\,M_\odot$	0.0037 ± 0.0021 [10]	0.072 ± 0.014 [10]	0.179 ± 0.022 [10]	0.032 ± 0.011 [10]	0.116 ± 0.023 [10]	0.549 ± 0.053 [10]

Figure 8. Distribution of peaks above 3σ in present-day galaxy-sized haloes. Line styles are as in Fig. 4. The circles in the upper left panel show the estimated mass and number density of wandering IMBHs assuming an $\mathcal{N} = 1$ seed hole for every 6×10^5 solar masses of 3σ progenitor halo material at $z_{0.9} = 17.9$, and a final black hole mass of $1.5 \times 10^4 \, M_\odot$ (see text for details).

competing effects of dynamical friction and tidal stripping within larger potential wells, as these complicated dynamical processes are dominated by the dark haloes that host the black holes. Therefore, in our toy model, the distribution of 3 or 3.5σ material at $z = 0$ describes the properties of holes wandering through within today's galaxy haloes. The predicted IMBH number density and mass density profiles are shown as circles in Figs 8 and 9: the former may be regarded as an upper limit since we have neglected black hole mergers, while the latter have been estimated assuming that these off-nuclear black holes have grown by accretion to a mean mass of $1.5 \times 10^4 \, M_\odot$, which is a rough estimate obtained from fig. 14 of Volonteri et al. (2003).

Depending on the IMF of Population III objects, some first-generation low-mass stars may have survived until today. Their number-density profile $n(r)$ within the Milky Way can again be read following the circles in Fig. 8, under the assumption that $\mathcal{N} = 1$ metal-free star survives for every 6×10^5 solar masses of 3σ progenitor halo material at $z_{0.9} = 17.9$. It is easy then to scale up the predicted value of $n(r)$ if $\mathcal{N} \gg 1$ such stars were to survive instead. On average, we find that about one-third of these remnants would lie today in the bulge, i.e. in the inner 3 kpc. This fraction fluctuates between 24 and 45 per cent in the four galaxies G0–G3. The density in the Solar neighbourhood is of the order of $\simeq 0.1 \, \mathcal{N} \, \text{kpc}^{-3}$, three orders of magnitude lower than in the bulge. The number density of remnants would be lower and more concentrated towards the

Galactic Centre if Population III stars only formed within rarer 3.5σ peaks (Fig. 9). On average, about 59 per cent of them would now lie within the bulge (range is 38–84 per cent) and the local number density would be only $\simeq 0.02 \, \mathcal{N} \, \text{kpc}^{-3}$. Even for $\mathcal{N} = 10$–100, this is an extremely small value, many orders of magnitude below the local number density of halo stars. *The above results suggest that the very oldest stars and their remnants should be best searched for within the Milky Way bulge.*

4.2 Stellar haloes

Material from $>2.5\sigma$ peaks has today a density profile that is very similar to the stellar halo around the Milky Way (Moore et al. 2005). It contributes a few per cent of the total virial mass, and therefore contains enough baryons to build up a $10^9 \, M_\odot$ stellar halo with a reasonable star formation efficiency. The assumption of a common pre-galactic origin between such a stellar component and the surviving Local Group dwarf galaxies provides an additional constraint and allows us to determine the progenitor mass threshold/redshift pair that best fits the data. From this argument Moore et al. (2005) identified hosts above $10^8 \, M_\odot$ at $z = 12$ as the progenitor haloes to which the bulk of halo stars originally belonged.

To check whether this simple model reproduces the kinematics as well as the radial distribution of halo stars, we have compared the predicted radial velocity dispersion profile with recent data
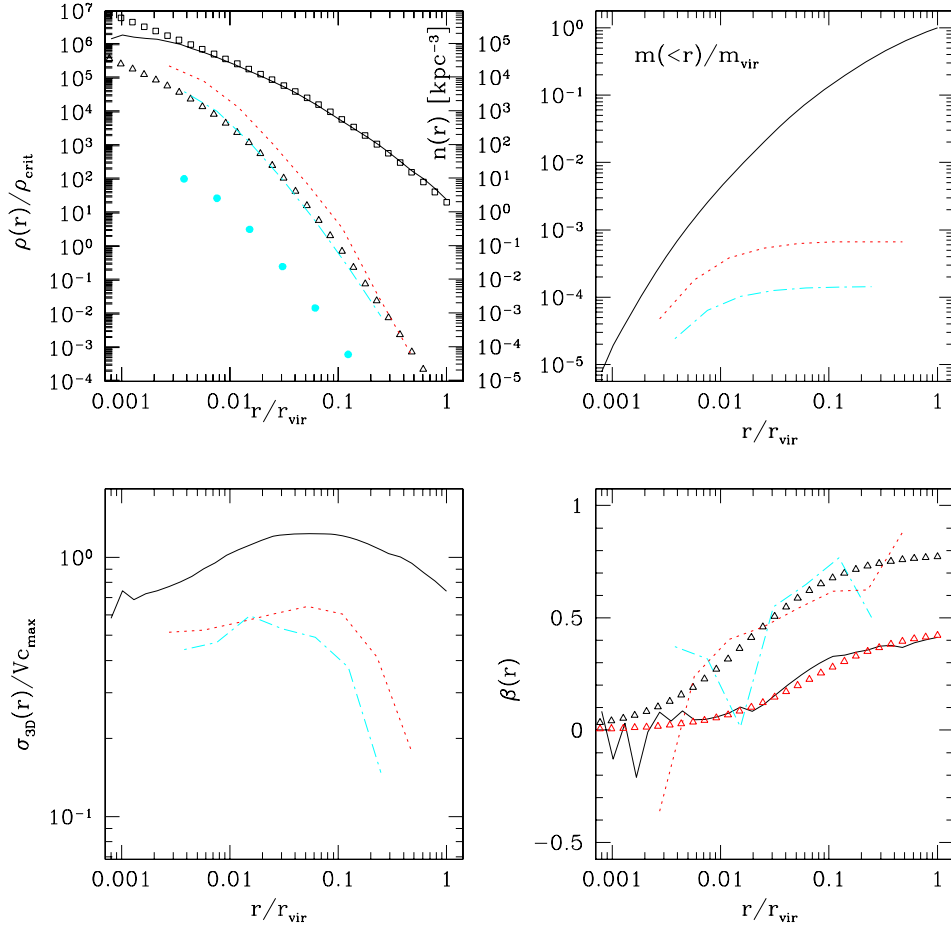
Figure 9. Same as Fig. 4 but for peaks above 3.5σ and for Population III progenitors collapsing at $z_{0.9} = 21.2$.

from Battaglia et al. (2005) (see Fig. 10). All haloes were rescaled (i.e. $r_{\rm vir} \rightarrow f r_{\rm vir}$, $V_{\rm c} \rightarrow f V_{\rm c}$, $M_{\rm vir} \rightarrow f^3 M_{\rm vir}$) to produce a local circular velocity of 220 km s^{-1} after taking into account the increase in circular velocity due to baryonic contraction [$V_{\rm c}(8.5\,{\rm kpc}) = 1.125\, V_{\rm c,max,DM}$] found by Macciò et al. (2005) for our halo G1. The rescaled virial masses are given in Fig. 10. The predicted $\sigma_{\rm r}$ (r) are close to the observed ones, especially for haloes G0 and G4. Our model predicts a radial anisotropy that grows with radius (see lower right panel of Fig. 10): in the Solar neighbourhood it gives $\sigma_{\rm 3D} \simeq V_{\rm c}$ and $\beta \simeq 0.4$, in good agreement with the observed values (Chiba & Beers 2000). The declining velocity dispersion near the centre is characteristic of haloes containing *only* dark matter. In the Galaxy we expect a flatter profile in the inner, baryon-dominated regions.

Both a high concentration ($c = 18$), highly anisotropic halo like G4 and a $c = 10$ halo with smaller anisotropy like G0 fit the data equally well. A detailed comparison requires knowledge of the tangential components of the velocity dispersion, in order to determine the concentration and virial mass of the Milky Way halo. The recently discovered stellar halo of M31 has a similar density profile to that of our Galaxy (Guhathakurta et al. 2005). The line-of-sight velocity dispersion observed in M31 is mostly due to tangential motions: preliminary results yield a constant $\sigma_{\rm t}/\sqrt{2}$ of about 80 km s^{-1} for $50 < r < 150$ kpc (Guhathakurta et al. 2005), close to the value expected for the G0 scenario but much higher than that of the G4 model. More data for M31 will hopefully soon become available, and many radial velocities of Milky Way halo stars will be obtained

by surveys like RAVE and SDSS-II. In the next decade the planned *GAIA* satellite will provide very detailed phase-space positions.

Another interesting feature of our model is that it predicts significant deviations from the simple radial velocity dispersion profiles expected for a smooth stellar halo in an NFW potential (like the models in fig. 4 of Battaglia et al. 2005). These deviations are evident in the upper right panel of Fig. 10 (but not in the lower left panel, where we show an average over four haloes).[2] The fluctuations are not an artefact of our analysis: with our usual choice of 30 logarithmic spherical bins out to the virial radius [similar to the binning of the observed $\sigma_{\rm r}(r)$] the fluctuations often extend over various bins, with each bin containing thousands of 'stars'. To show fluctuations of $\sigma_{\rm r}(r)$ on smaller scales we have binned 'stars' in halo G0 using linear spherical bins, and have plotted the resulting $\sigma_{\rm r}(r)$ profile in the same radial range of the observations (circles with error bars in the upper right panel of Fig. 10). The linear bins contain at least 108 stars; the error bars represent Poisson noise. We have also plotted $\sigma_{\rm 3D,DM}(r)$ of halo G0 twice using different bin sizes. Note that the velocity dispersion of the dark matter halo as a whole (instead of the material belonging to the $>2.5\sigma$ $z = 12$ subset) in our simulated

---

[2] The sample from Battaglia et al. (2005) and our G4 outer stellar halo contain similar numbers of 'stars'. Both have relatively large Poisson noise and are consistent with smooth $\sigma_{\rm r}(r)$ profiles. In haloes resolved with more particles like G0–G3 and D12, the 'stellar' radial velocity dispersions are clearly inconsistent with smooth profiles.
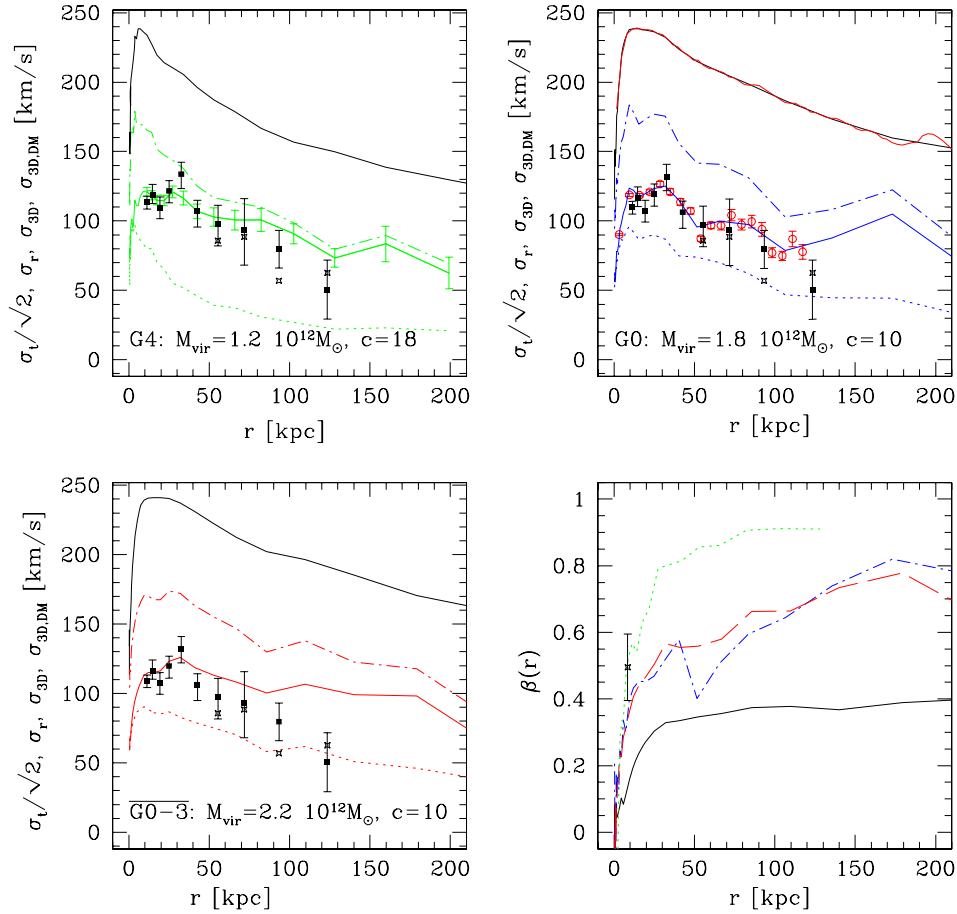
Figure 10. Kinematics of our model stellar haloes compared with observations of Milky Way halo stars. The simulated CDM haloes are rescaled to give a local circular velocity of 220 km s^{-1} after taking baryonic contraction into account (see text for details). The lower right panel shows the predicted anisotropy profiles $\beta(r) = 1 - \sigma_t^2(r)/2\sigma_r^2(r)$ for the G0–G3 average halo (dashed line: halo 'stars'; solid line: dark matter) and for halo stars in G0 (dash-dotted) and G4 (dotted). The data point is the local halo anisotropy from Chiba & Beers (2000). The curves in the other three panels show, from bottom to top, the 'stellar' $\sigma_t/\sqrt{2} \simeq \sigma_\theta \simeq \sigma_\phi$ (dotted line), σ_r (solid line) and σ_{3D} (dash-dotted line). The uppermost solid curve depicts the 3D velocity dispersion profile of the dark matter (note that it is much larger and smoother than the stellar σ_{3D}). To illustrate the fluctuations in the stellar dispersions, σ_r and $\sigma_{3D,DM}$ in halo G0 are plotted twice: once using our usual choice of 30 logarithmic bins to the virial radius, and once using smaller linear bins (open circles with Poissonian error bars for σ_r, another solid line for $\sigma_{3D,DM}$). The points are the measured σ_r of Milky Way halo stars from Battaglia et al. (2005), with (squares) and without (stars) the contribution from satellite galaxies. The error bars reflect only the accuracy of the observations, while Poisson noise (which causes similar, in some bins even larger, errors) is not included. The declining dispersions near the centre are characteristic for halo containing *only* dark matter. In the Galaxy we expect a flatter profile in the inner, baryon-dominated regions.

galaxies is generally a smooth function of radius, with small deviations becoming apparent only at $r \sim 200$ kpc. As fluctuations in the stellar $\sigma_r(r)$ are not caused by mass bound to subhaloes (the mass fraction is much too small particularly within the inner halo), this leaves tidal streams as the most probable cause of such deviations. The entire dark halo is assembled from about 10^5 resolved progenitors, the tidal debris of which are well mixed and smooth. In our model, the stellar halo is made up instead from only a few hundred building blocks (and a significant fraction of it comes from the most massive ones), and is therefore expected to show some granularity. A more detailed study of tidal features in our model stellar haloes is left to a future paper.

4.2.1 Comparison to recent related models for the formation of the stellar halo

During the completion of this work two related models for the formation of the stellar halo (Bullock & Johnston 2005; Abadi, Navarro

& Steinmetz 2005) came to our attention. Both studies are more detailed than ours in the sense that they try to model the effect of star formation and chemical evolution. Bullock & Johnston (2005) use a semi-analytic approach combined with *N*-body simulations of satellite disruption in an external, growing galaxy potential. As in this work, the number of luminous satellites and the mass of the final stellar halo are adjusted to match the observations by assuming that reionization suppresses star formation in later-forming small progenitors. Our stellar haloes, however, seem to be more concentrated than those of Bullock & Johnston (2005). This may due to the fact that we only trace old stellar populations, while Bullock & Johnston also allow for more recent episodes of star formation in their protogalactic building blocks. They also model the disruption of satellites assuming an external spherical potential: this is probably a good approximation to recent accretion events that build up the outer stellar halo. The inner stellar halo, however, is built up through a series of early, major mergers: these cause rapid potential fluctuations (violent relaxation) which are not accounted for in the

spherical potential approximation. This limitation was also pointed out by Bullock & Johnston (2005).

The cosmological SPH simulations of Abadi et al. (2005), while not including any global mechanism for suppressing star formation in later-forming small progenitors, do lead to similar stellar halo profiles and kinematics as our model. They seem to produce, however, far too many halo stars: recent SPH simulations at higher resolution and without strong feedback effects also overpredict the number of satellites by a large factor Macció et al. (2005) and tend to produce even more halo stars. The similarity of the profile shape and kinematics of stellar haloes in all these models suggests that they are a robust and generic outcome of hierarchical structure formation (see also Hansen & Moore 2005; Dekel et al. 2005) and do not depend on the detailed formation history. Note that this does not contradict our argument about the possibility of using the radial extent of collisionless tracer populations to learn about their formation epoch and sites. It just illustrates how this argument is limited to fossil records from very high redshift ($z > 8$, see also Section 2.2). At lower redshifts the typical haloes are larger and the exact star formation sites must be taken into account. Efficient cooling (and/or numerical losses of gas angular momentum to the dark matter in under-resolved progenitors) can produce a population of stars at some intermediate redshift with a distribution that is similar to much older populations from early high-σ peaks. By $z = 0$ the two subsets would have very similar concentrations and

kinematics, which might explain the similar results found here and in Abadi et al. (2005).

4.3 Metal-poor globular clusters

The clustering properties of metal-poor globular clusters contain clues on their formation sites and the epoch when star formation was suppressed by feedback processes (e.g. reionization, supernova-driven winds) in low-mass haloes. In the Milky Way metal-poor globular clusters follow the same radial profile as halo stars, suggesting within the framework of our model a common origin within early 2.5σ peak progenitors at $z \approx 12$. Observations of the distribution of globular clusters within present-day haloes of different masses could provide information on feedback effects as a function of environment (Moore et al. 2005). The suppression of globular cluster formation at some early epoch may also explain the bimodality observed in cluster metallicities (e.g. Strader et al. 2005). The widely used assumption that globular cluster formation is a fair tracer of star formation, combined with the suppression of the formation of metal-poor globulars after reionization, imply that the amount of high-σ material in a halo is proportional to the number of metal-poor globular clusters. From the results in Section 3.4 it follows then that a simple universal reionization epoch would lead to a constant abundance of metal-poor globular clusters per virial mass. Deviations from this simplest case may provide information about
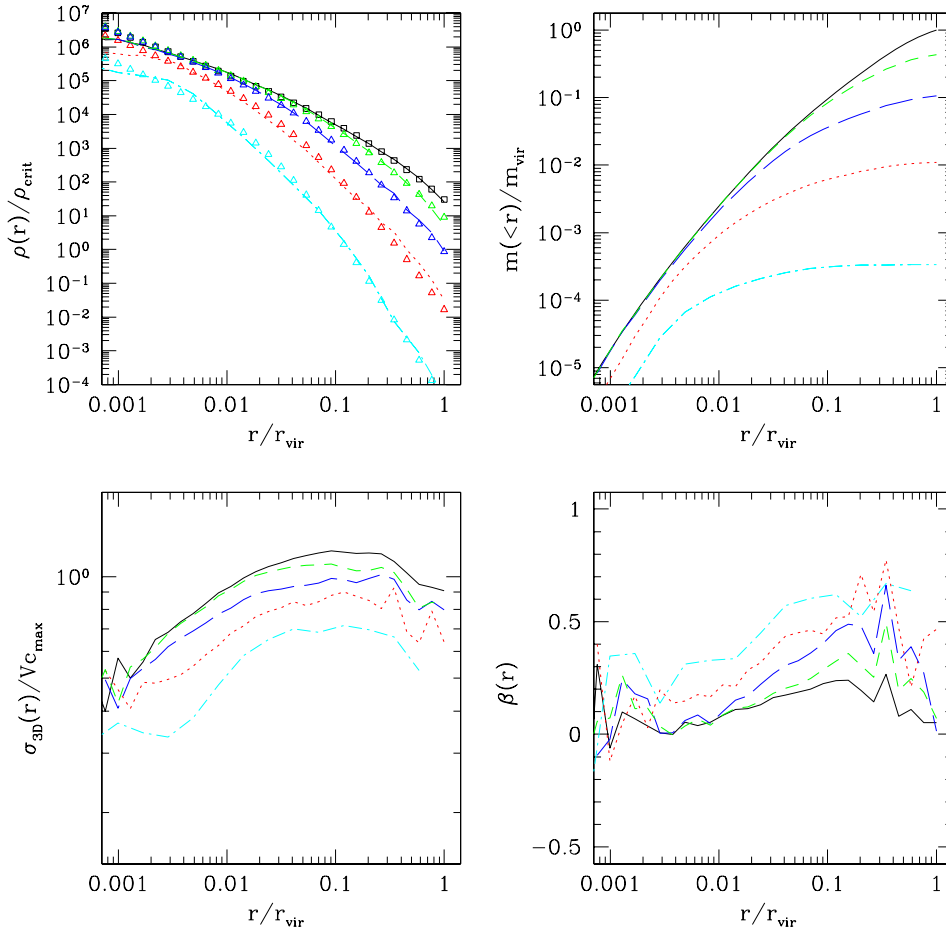
Figure 11. Distribution of peaks above 1 (short-dashed), 2 (long-dashed), 3 (dotted) and 4σ (dash-dotted) in a present-day cluster-sized halo ($M_{\rm vir} = 3.1 \times 10^{14}\,{\rm M}_\odot$). The redshift and minimum mass pairs used are ($z = 1.6$, $7.4 \times 10^9\,{\rm M}_\odot$) for the 1$\sigma$ peaks, (4.4, $6.3 \times 10^9\,{\rm M}_\odot$) for the 2$\sigma$, ($7.4$, $4.3 \times 10^9\,{\rm M}_\odot$) for the 3$\sigma$, and ($8.7$, $1.8 \times 10^{10}\,{\rm M}_\odot$) for the 4$\sigma$ peaks. The triangles in the upper left panel show the fitting function (2).
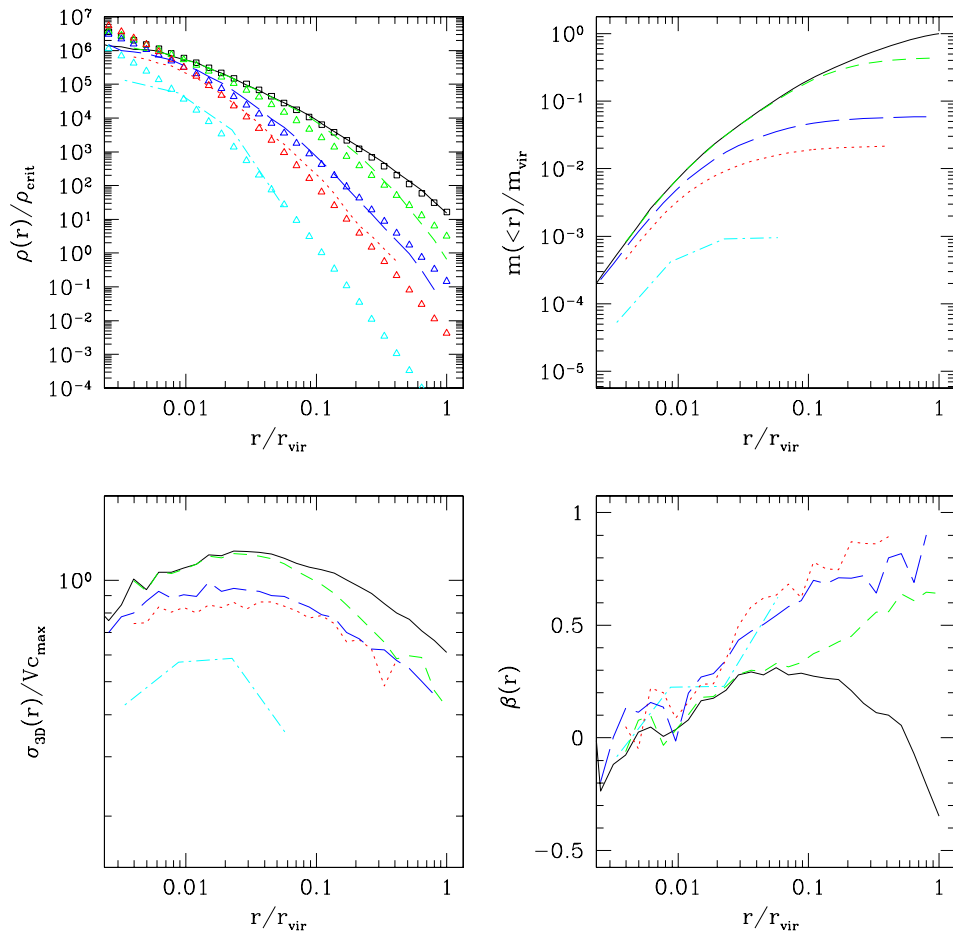
Figure 12. Same as Fig. 4 for peaks above 1 (short-dashed), 2 (long-dashed), 3 (dotted) and 3.5σ (dash-dotted) in a small galaxy halo ($M_{vir} = 10^{11}\,M_\odot$) at $z = 0$. The redshift and minimum mass pairs used are ($z = 2.4$, $4.8 \times 10^8\,M_\odot$) for the 1σ peaks, (8.7, $7.6 \times 10^6\,M_\odot$) for the 2σ, (10.5, $2.2 \times 10^8\,M_\odot$) for the 3σ, and (13.7, $4.9 \times 10^7\,M_\odot$) for the 3.5σ peaks. The triangles in the upper left panel show the fitting function (2).

the local reionization epoch, and whether regions with more (less) metal-poor globulars per virial mass were reionized later (earlier) (see Moore et al. 2005).

4.4 Elliptical galaxies

The projected luminosity profiles of elliptical galaxies follow the $R^{1/4}$ law and resemble rescaled versions of projected CDM halo density profiles (Łokas & Mamon 2001; Merrit et al. 2005), similar to the $z = 0$ profiles of our high-σ subsets. Ordinary elliptical galaxies may form by multiple mergers or by the major merger of two disc galaxies (e.g. Dekel et al. 2005). Early formation ($z \simeq 6$) in a large number of progenitors followed by a series of gas-poor, essentially collisionless mergers could build up the giant ellipticals (cD) in the centres of galaxy clusters. These mergers might undo some of the early dissipational contraction of the total mass distribution (Gao et al. 2004).

Fig. 11 shows the distribution of material belonging to different σ peaks in a $z = 0$ cluster halo. The inner cluster regions are entirely made up of material from $>2\sigma$ peaks, and this selection contributes about 10 per cent to the cluster virial mass. The central brightest galaxies in SDSS clusters have an average effective radius of $R_e \simeq$ 20 kpc and presumably about 10 per cent of the cluster luminosity (Zibetti et al. 2005). Our 2σ subsets contain enough mass to account for the observed cD luminosities, but they are more extended. If the

cD stars formed early in the inner parts of all progenitor haloes above 2σ, then they would be found closer to the cluster centre today (see Section 2.2). A simple way to select the inner parts of 2σ progenitors is to mark higher-σ peaks at earlier epochs. Our 3σ selections have a realistic effective radius of about 20 kpc. Therefore we predict the kinematics of the average brightest cluster galaxies to follow the 3σ selections shown in Fig. 11 if (or where) the real cluster potentials are similar to the uncontracted potentials formed in dissipationless cosmological simulations (as suggested by Gao et al. 2004).

The anisotropy of a $z = 0$ subset depends mostly on its density profile shape (or ν) and not on the selection redshift or the number of mergers it has undergone (Figs 4 to 9). A few mergers are enough to establish the general $\beta(r)$ profile (8) and the slope–anisotropy relation (Section 3.2.3). This agrees with Moore et al. (2004), who find $\beta \simeq 0.5$ after only one low angular momentum merger of initially isotropic CDM haloes (see also Hansen & Moore 2005). Dekel et al. (2005) also find a similar $\beta(r)$ profile after only one merger, which even starts with disc galaxies, i.e. nearly circular initial orbits for the stars (see their β for the old stars; fig. 1 of Dekel et al. 2005). Their average anisotropy at the half-mass radius of the old stellar component is $\beta = 0.3$, which is lower than our average of $\beta = 0.45$; but, considering the very different initial conditions of the stars and the larger numbers of mergers in our cosmological context, the results are surprisingly similar. Therefore we argue that our collisionless results are relevant both for giant elliptical galaxies which formed

in a series of dissipation-less mergers (Gao et al. 2004) and also for the old stars in smaller ellipticals.

The general relation between density profile slope and anisotropy for high-σ subsets $\beta(\mathrm{d}\log\rho/\mathrm{d}\log r) \simeq -0.23(1.2 + \mathrm{d}\log\rho/\mathrm{d}\log r)$ can be applied to elliptical galaxies to infer $\beta(r)$ from the observed stellar profile. This is useful to obtain dynamical mass estimates for elliptical galaxies, where one has to assume some $\beta(r)$ (Mamon & Łokas 2005) and it is probably the best guess before realistic, cosmological, hydrodynamical simulations of elliptical galaxy formation become available.

5 CONCLUSIONS

We have used high-resolution cosmological *N*-body simulations to trace the spatial distribution and kinematics in present-day CDM haloes of collisionless material that originally belonged to selected branches of the merger hierarchy. Our main results can be summarized as follows.

(i) Hierarchical merging does not efficiently mix haloes up. The final distribution of dark matter particles retains a memory of when and where they collapsed initially, allowing a unique test of the popular bottom-up paradigm for the formation of cosmic structure.

(ii) Today's distribution and kinematics of halo substructure that formed at very high redshift depend mostly on the rarity of the primordial density fluctuations to which they correspond. For example, the $z = 0$ density, shape, anisotropy and velocity dispersion profiles of material originating from early 3σ peaks is independent of the redshift/minimum mass pair used to select it. The mass fractions within the parent host, however, grow if such particles are chosen from lower-redshift progenitors at a higher mass threshold.

(iii) High-σ material should be looked for close to the centre of massive parent haloes. The concentration and outer slope of the mass-density profile are larger for the rarer peaks.

(iv) The anisotropy increases faster with radius for material originating within rarer peaks (equation 8). The parameter $\beta(r)$ steepens with increasing ν at the same rate as the half-mass radius shrinks, i.e. we generally find $\beta(r_{1/2}) \simeq 0.45$.

(v) Velocity dispersions are lower for material from the rarer peaks, and particle orbits are more radial. While the average velocity dispersion profiles agree with stationary solutions to the Jeans equation (4), the profiles of individual haloes show significant structure and are inconsistent with smooth $\sigma(r)$ solutions (see Fig. 10).

(vi) The high-σ subsets have much more elongated shapes than their host haloes. For 3σ material the mean c/a is about 0.35, while present-day galaxy-size haloes have a mean of 0.6.

(vii) These properties do not depend on which regions within early ($z > 8$) progenitors are marked and traced to the present time. Particles originating within the cores of high-σ progenitors are distributed at $z = 0$ in the same way as the entire virial mass of these early structures. This is not true at later epochs, where the marking of only the densest progenitor regions results in more concentrated density profiles (e.g. the selection of only the densest 10 per cent of the mass of progenitor haloes above 1σ at $z = 1.6$ yields a present-day distribution similar to that of all particles above 2σ).

(viii) If the first stars form at early epochs in peaks above 3.5σ, then half of their remnants should be found in the bulge, within 3 kpc of the Galactic Centre. In the Solar neighbourhood, the density of such a very old population is 1000 times lower than in the bulge. Also, their characteristic velocities are 2.5 times lower than those of dark matter particles, and their orbits more radial ($\beta \simeq 0.5$).

(ix) The radial profile of the stellar halo and metal-poor globular clusters of the Milky Way suggest that these components formed in rare early peaks above 2.5σ at redshift above 10. Typical outer halo objects have radial orbits, and become isotropic near the Galactic Centre.

(x) Radial orbits are a general outcome for any concentrated stellar component assembled through gas-poor mergers. The anisotropy parameter $\beta(r, \nu)$ correlates well with $\rho(r, \nu)$ and is not sensitive to the detailed assembly history of such a component.

The applications discussed above should be taken as a first attempt at predicting the spatial distribution and kinematics in present-day galaxies of objects that formed within early protogalactic systems, all in the context of hierarchical structure formation theories. Some interesting directions for future work may include, for example, combining spatial information on Population III remnants with semi-analytic prescriptions for the growth and dynamical evolution of black holes, as well as using chemical evolution models to translate the age gradient for stellar haloes found here into metal abundance gradients. The techniques presented here also allow one to study the properties of stellar streams in realistic, triaxial, clumpy CDM galaxy haloes.

REFERENCES

Abadi M. G., Navarro J. F., Steinmetz M., 2005, MNRAS, submitted (astro-ph/0506659)
Abel T., Bryan G. L., Norman M. L., 2000, ApJ, 540, 39
Bailin J., Steinmetz M., 2005, ApJ, 627, 647
Battaglia G. et al., 2005, MNRAS, in press (doi:10.1111/j.1365-2966.2005.09367.x) (astro-ph/0506102)
Binney J., Tremaine S., 1987, Galactic Dynamics. Princeton Univ. Press, Princeton, NJ
Bromm V., Coppi P. S., Larson R. B., 2002, ApJ, 564, 23
Bullock J. S., Johnston K. V., 2005, ApJ, submitted (astro-ph/0506467)
Bullock J. S., Kravtsov A. V., Weinberg D. H., 2000, ApJ, 539, 517
Chiba M., Beers T. C., 2000, AJ, 119, 2843
Cole S., Kaiser N., 1989, MNRAS, 237, 1127
Davis M., Efstathiou G., Frenk C. S., White S. D. M., 1985, ApJ, 292, 371
Dekel A., Stoehr F., Mamon G. A., Cox T. J., Primack J. R., 2005, Nat, 437, 707
Diemand J., Moore B., Stadel J., Kazantzidis S., 2004a, MNRAS, 348, 977
Diemand J., Moore B., Stadel J., 2004b, MNRAS, 352, 535
Diemand J., Moore B., Stadel J., 2004c, MNRAS, 353, 624
Diemand J., Zemp M., Moore B., Stadel J., Carollo M., 2005, MNRAS, in press (doi:10.1111/j.1365-2966.2005.09601.x) (astro-ph/0504215)
Dubinski J., Carlberg R. G., 1991, ApJ, 378, 496
Faltenbacher A., Kerscher M., Gottloeber S., Mueller V., 2002, A&A, 395, 1

Gao L., Loeb A., Peebles P. J. E, White S. D. M., Jenkins A., 2004, ApJ, 614, 17

Ghigna S., Moore B., Governato F., Lake G., Quinn T., Stadel J., 1998, MNRAS, 300, 146

Guhathakurta P., Ostheimer J. C., Gilbert K. M., Rich R. M., Majewski S. R., Kalirai J. S., Reitzel D. B., Patterson R. J., 2005, Nat, submitted (astro-ph/0502366)

Hansen S. H., Moore B., 2005, MNRAS, submitted (astro-ph/0411473)

Jing Y. P., Suto Y., 2002, ApJ, 574, 538

Katz N., 1991, ApJ, 368, 325

Kuhlen M., Madau P., 2005, MNRAS, 363, 1069

Lacey C., Cole S., 1993, MNRAS, 262, 627

Łokas, E. L., Mamon, G. A., 2001, MNRAS, 321, 155

Madau P., Rees M. J., 2001, ApJ, 551, L27

Mamon G. A., Łokas E. L., 2005, MNRAS, 363, 705

Márquez I., Lima Neto G. B., Capelato H., Durret F., Lanzoni B., Gerbal D., 2001, A&A, 379, 767

Merritt D., Navarro J. F., Ludlow A., Jenkins A., 2005, ApJ, 624, L85

Moore B., 2001, in Wheeler J. C., Martel H., eds, AIP Conf. Proc. Vol. 586, 20th Texas Symp. on Relativistic Astrophysics. Am. Inst. of Phys., New York, p. 73

Moore B., Governato F., Quinn T., Stadel J., Lake G., 1998, ApJ, 499, L5

Moore B., Quinn T., Governato F., Stadel J., Lake G., 1999, MNRAS, 310, 1147

Moore B., Kazantzidis S., Diemand J., Stadel J., 2004, MNRAS, 354, 522

Moore B., Diemand J., Madau P., Zemp M., Stadel J., 2005, MNRAS, submitted (astro-ph/0510370)

Navarro J. F., Frenk C. S., White S. D. M., 1996, ApJ, 462, 563

Sheth R. K., Tormen G., 1999, MNRAS, 308, 119

Springel V., White S. D. M., Tormen G., Kauffmann G., 2001, MNRAS, 328, 726

Stadel J., 2001, PhD thesis, Univ. Washington

Strader J., Brodie J. P., Cenarro A. J., Beasley M. A., Forbes D. A., 2005, AJ, 130, 1315

van den Bosch F. C., Yang X. H., Mo H. J., Norberg P., 2005, MNRAS, 356, 1233

Volonteri M., Haardt F., Madau P., 2003, ApJ, 582, 559

White S. D. M., Springel V., 2000, in Weiss A., Abel T., Hill V., eds, The First Stars. Springer, Heidelberg, p. 327

Yoshida N., Abel T., Hernquist L., Sugiyama N., 2003, ApJ, 592, 645

Zibetti S., White S. D. M., Schneider D. P., Brinkmann J., 2005, MNRAS, 358, 949

This paper has been typeset from a TEX/LATEX file prepared by the author.